Comparison of Tripolar and Circular Pads for IPT Charging Systems

Seho Kim, *Student Member, IEEE*, Grant A. Covic, *Senior Member, IEEE*, and John T. Boys

***Abstract*—Recently, a magnetic pad called the tripolar pad (TPP) has been introduced for inductive power transfer (IPT) systems. This paper evaluates the effective coupling factor and leakage magnetic field of a 20-kW IPT system that uses a combination of TPP and circular pad (CP) topologies over a range of lateral displacements. The results show that the effective coupling factor and the leakage magnetic field of the TPP–TPP system are substantially better when the secondary is displaced away from ideal alignment. Leakage magnetic field is reduced up to 43% compared to the CP–CP system at the worst-case misalignment, which is due to the ability of the TPP–TPP system to generate and capture different types of magnetic field shapes. Simulation methods for both the TPP and CP are validated in the laboratory using a 2-kW system operating at 85 kHz.**

***Index Terms*—Coupling circuits, electromagnetic coupling, magnetic circuits, magnetic resonance.**

I. Introduction

INDUCTIVE power transfer (IPT) is a method of coupling power across an air gap without any physical contacts [1]–[4]. IPT systems have been used in numerous applications including battery charging, automated guided vehicles, lighting, and material handling [5]–[10]. An example of a typical IPT system is shown in Fig. 1.

One of the most important aspects of IPT systems is the design of the magnetic structures. The magnetic structures of an IPT system determine the power transfer capability as well as the extent to which the leakage magnetic field (B_{leak}) is controlled during operation. B_{leak} is the unwanted stray magnetic field generated by an IPT system during power transfer, which needs to be minimized, in case it is harmful to people [11].

Numerous magnetic structures have been designed for IPT systems in the past including solenoids, circular pads (CP), double-D pads (DDP), double-D quadrature pads, and bipolar pads (BPP) [12]–[31]. One of the recently proposed magnetic structures is the tripolar pad (TPP). The TPP was introduced previously as a primary pad for an IPT system and evaluated against both CP and BPP secondaries [32].

Manuscript received March 15, 2017; revised June 3, 2017 and August 7, 2017; accepted August 7, 2017. Date of publication August 16, 2017; date of current version March 5, 2018. Recommended for publication by Associate Editor C. K. Tse. *(Corresponding author: Seho Kim.)*

The authors are with the Department of Electrical and Computer Engineering, The University of Auckland, Auckland 1010, New Zealand (e-mail: skim281@aucklanduni.ac.nz; ga.covic@auckland.ac.nz; j.boys@auckland.ac.nz).

Color versions of one or more of the figures in this paper are available online at http://ieeexplore.ieee.org.

Digital Object Identifier 10.1109/TPEL.2017.2740944

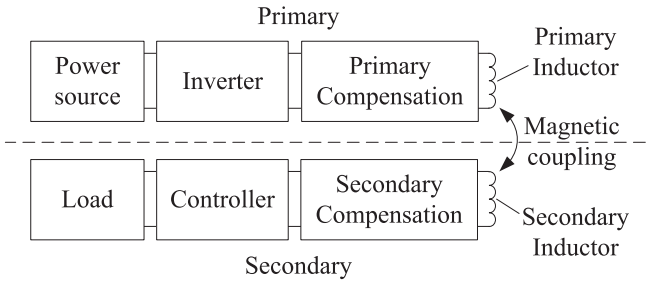

Fig. 1. Overview of a typical IPT system.

In this paper, the suitability of the TPP as both the primary pad and the secondary pad is investigated for higher levels of power transfer and compared against a more traditional system using a CP primary and a CP secondary with similar dimensions and volumes of material. This paper begins with mathematical models describing the operation of an IPT system using a CP primary and a CP secondary (CP–CP). This mathematical model is then expanded to describe an IPT system with a TPP primary and a TPP secondary (TPP–TPP). Using the derived mathematical models, an exhaustive search controller is devised to find the optimal primary currents that result in the highest effective coupling factor (k_{eff}) for all secondary displacements. With the controller, the performance of the CP–CP, CP–TPP, TPP–CP, and TPP–TPP systems is simulated in terms of k_{eff} and B_{leak} for a power output of 20 kW at 85 kHz under various alignment and misalignment conditions. A prototype TPP–TPP system is implemented in the laboratory for power output of 2 kW at 85 kHz to validate the simulation findings.

II. IPT System Overview

A fundamental IPT circuit can be shown in Fig. 2(a) as open-circuited and (b) short-circuited.

Here, V_{p} and I_{p} denote the voltage and current in the primary coil, and L_{p} and L_{s} are the primary and secondary inductors. M_{ps} is the mutual inductance between the primary and the secondary coils. M_{ps} is determined by $M_{\mathrm{ps}} = k\sqrt{L_{\mathrm{p}} L_{\mathrm{s}}}$, where k refers to the traditional coupling factor between L_{p} and L_{s}. Given the circuits shown in Fig. 2, the open-circuit voltage V_{oc} and short-circuit current I_{sc} can be determined as

$$V_{\mathrm{oc}} = j\omega M_{\mathrm{ps}} I_{\mathrm{p}} \tag{1}$$

$$I_{\mathrm{sc}} = \frac{M_{\mathrm{ps}}}{L_{\mathrm{s}}} I_{\mathrm{p}}. \tag{2}$$

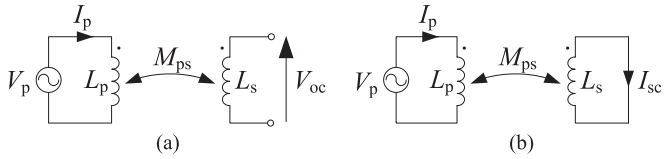

Fig. 2. Two-coil IPT circuit depicting (a) open-circuit voltage and (b) short-circuit current.

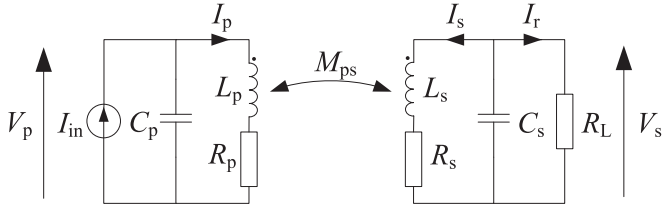

Fig. 3. Circuit diagram of an IPT system with CP as primary and secondary.

Here, ω is the operating frequency of the IPT system. From (1) and (2), the uncompensated apparent power output S_{u} can be found

$$S_{\mathrm{u}} = V_{\mathrm{oc}} I_{\mathrm{sc}} = \omega \frac{M_{\mathrm{ps}}^2}{L_{\mathrm{s}}} I_{\mathrm{p}}^2 = \omega L_{\mathrm{p}} I_{\mathrm{p}}^2 k^2. \tag{3}$$

IPT systems are tuned to improve power transfer capabilities between the primary and the secondary. A typical parallel-tuned circuit for an IPT system using a single-coil primary and a single-coil secondary is shown in Fig. 3.

Assuming that the tuning is ideal and the operating frequency stays constant, the values of the primary and secondary tuning capacitors C_{p} and C_{s} can be determined using $\omega = 1/\sqrt{LC}$. Here, the loaded quality factor of the parallel-tuned secondary circuit (Q_{s}) is $Q_{\mathrm{s}} = R_{\mathrm{L}}/(\omega L_{\mathrm{s}})$ and the impedances of the primary and secondary circuits are given by $Z_{\mathrm{p}} = j\omega L_{\mathrm{p}} + R_{\mathrm{p}}$ and $Z_{\mathrm{s}} = j\omega L_{\mathrm{s}} + R_{\mathrm{s}} + 1/(j\omega C_{\mathrm{s}} + 1/R_{\mathrm{L}})$.

The operations of the circuit can be shown in a matrix form as

$$\begin{bmatrix} V_{\mathrm{p}} \\ 0 \end{bmatrix} = \begin{bmatrix} Z_{\mathrm{p}} & j\omega M_{\mathrm{ps}} \\ j\omega M_{\mathrm{ps}} & Z_{\mathrm{s}} \end{bmatrix} \begin{bmatrix} I_{\mathrm{p}} \\ I_{\mathrm{s}} \end{bmatrix}. \tag{4}$$

From the matrix, some useful equations can be found.

$$V_{\mathrm{p}} = \left(Z_{\mathrm{p}} + \frac{\omega^2 M_{\mathrm{ps}}^2}{Z_{\mathrm{s}}} \right) I_{\mathrm{p}} \tag{5}$$

$$V_{\mathrm{s}} = \frac{1}{j\omega C_{\mathrm{s}} + \frac{1}{R_{\mathrm{L}}}} I_{\mathrm{s}} \tag{6}$$

$$I_{\mathrm{s}} = \frac{-j\omega M_{\mathrm{ps}}}{Z_{\mathrm{s}}} I_{\mathrm{p}} \tag{7}$$

$$I_{\mathrm{r}} = \frac{1}{jQ_{\mathrm{s}} + 1} I_{\mathrm{s}} \tag{8}$$

$$S_{\mathrm{p}} = |V_{\mathrm{p}}||I_{\mathrm{p}}| \tag{9}$$

$$S_{\mathrm{s}} = |V_{\mathrm{s}}||I_{\mathrm{s}}| \tag{10}$$

$$P_{\mathrm{out}} = |V_{\mathrm{s}} I_{\mathrm{r}}| = S_{\mathrm{u}} Q_{\mathrm{s}} = S_{\mathrm{p}} k^2 Q_{\mathrm{s}}. \tag{11}$$

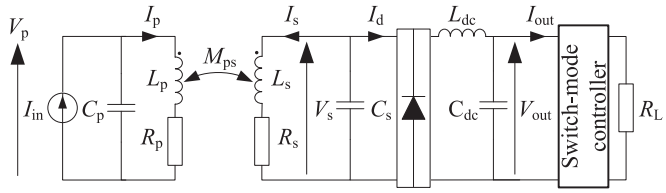

Fig. 4. Circuit diagram of an IPT system with a diode bridge and switch-mode controller in the secondary.

Here, V_{p} is the voltage across the primary inductor with considerations to the magnetic losses in the primary and the reflected impedances from the secondary. V_{s} and I_{s} are the voltage and current induced in the secondary inductor. I_{r} is the current in the load resistor R_{L}. S_{p} and S_{s} are the apparent power in the primary and the secondary inductors, respectively. While only parallel-tuned systems are investigated in this paper, all equations can be converted to series-tuned systems.

In practice, battery charging applications for IPT systems commonly require the output to be converted to dc. A full-bridge rectifier can be added to the circuit in Fig. 3 resulting in the circuit shown in Fig. 4.

Under ideal assumptions of continuous conduction and zero losses through this bridge rectifier, the addition of the rectifier results in the following voltage and the current relationships between the fundamental rms components of the ac waveforms (6) and (8) and the resulting dc voltages and currents represented as I_{out} shown in (12) and (13). In this paper, only the fundamental harmonic is considered for the analysis

$$V_{\mathrm{out}} = \left| \frac{2\sqrt{2}}{\pi} V_{\mathrm{s}} \right| \tag{12}$$

$$I_{\mathrm{out}} = \left| \frac{\pi}{2\sqrt{2}} I_{\mathrm{r}} \right| \tag{13}$$

$$P_{\mathrm{out}} = V_{\mathrm{out}} I_{\mathrm{out}}. \tag{14}$$

A switch-mode controller is added as shown in Fig. 4 to regulate V_{out} depending on the output requirements, such as the ratings of a battery. This means that according to (12), V_{s} depends on what the switch-mode controller regulates V_{out} to be. Then, Q_{s} can be found as

$$Q_{\mathrm{s}} = \frac{|V_{\mathrm{s}}|}{|V_{\mathrm{oc}}|} = \frac{|\frac{\pi}{2\sqrt{2}} V_{\mathrm{out}}|}{|j\omega M_{\mathrm{ps}} I_{\mathrm{p}}|}. \tag{15}$$

Given that V_{out} is fixed, Q_{s} is shown to be a function of mutual inductance between the primary and secondary coils and the current in the primary coil.

Equations (4)–(15) can be expanded for an IPT system with a TPP primary and a TPP secondary. In this case, there are three primary coils and three secondary coils, as shown in Fig. 5. Note that the subscript "p" and "s" are used to indicate the different primary and secondary coils in the system. In a TPP, the three coils are partially overlapped with each other by design similar to the BPP [32]–[34] so that when one of the TPP coils is energized, the adjacent coils have no net EMF induced in

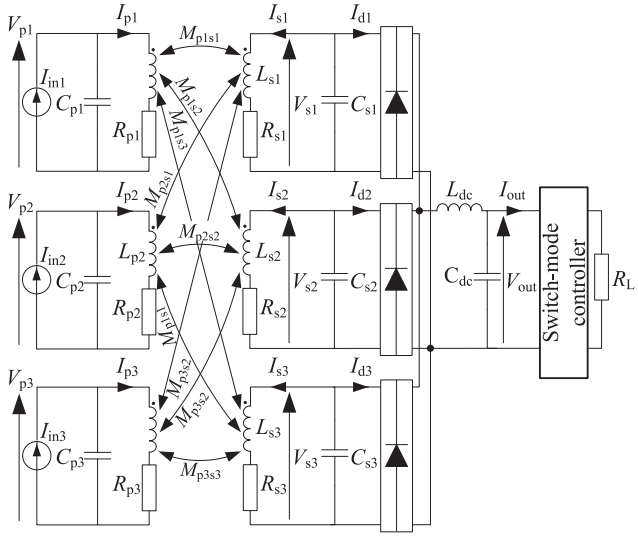

Fig. 5. Circuit diagram of an IPT system with TPP as primary and secondary.

them. Under these conditions, the coils are said to be mutually decoupled. Since these works have shown that the mutual cross coupling between the coils of the same pad is low, these can be neglected in practice and are not shown in Fig. 5.

From the system shown in Fig. 5, the matrix from (4) can be expanded as shown in (16) at the bottom of this page. The natural independence of the coils in each of the TPP results in a matrix shown in (16), which has many of the terms set to zero. This simplifies the analysis and the operation of the system compared to other three coil topologies in the literature, where a detailed analysis of all the implications of the three coil cross coupling in the primary and the three coils in the secondary is required. Further elaborations requiring the analysis of a TPP primary without ideal mutual decoupling between the TPP coils can be found in [32].

From the matrix in (16), some useful equations for this TPP primary to TPP secondary system can be found

$$V_{\mathrm{sn}} = \frac{\pi}{2\sqrt{2}} V_{\mathrm{out}} \tag{17}$$

$$V_{\mathrm{ocn}} = \sum_{m=1}^{3} j\omega M_{\mathrm{pmsn}} I_{\mathrm{pm}} \tag{18}$$

$$I_{\mathrm{scn}} = \frac{V_{\mathrm{ocn}}}{j\omega L_{\mathrm{sn}}} \tag{19}$$

$$Q_{\mathrm{sn}} = \frac{V_{\mathrm{sn}}}{V_{\mathrm{ocn}}} = \frac{\frac{\pi}{2\sqrt{2}} V_{\mathrm{out}}}{\sum_{m=1}^{3} j\omega M_{\mathrm{pmsn}} I_{\mathrm{pm}}} \tag{20}$$

$$I_{\mathrm{sn}} = -(jQ_{\mathrm{sn}} + 1) I_{\mathrm{scn}} \tag{21}$$

$$I_{\mathrm{out}} = \frac{\pi}{2\sqrt{2}} \left| \sum_{n=1}^{3} I_{\mathrm{scn}} \right| \tag{22}$$

$$V_{\mathrm{pm}} = Z_{\mathrm{pm}} I_{\mathrm{pm}} + \sum_{n=1}^{3} j\omega M_{\mathrm{pmsn}} I_{\mathrm{sn}} \tag{23}$$

$$S_{\mathrm{p\ total}} = \sum_{m=1}^{3} (|V_{\mathrm{pm}}||I_{\mathrm{pm}}|) \tag{24}$$

$$P_{\mathrm{out}} = |V_{\mathrm{out}}||I_{\mathrm{out}}|. \tag{25}$$

The subscripts "m" and "n" in (23)–(24) is used to denote different TPP primary or secondary coils, respectively. Since three separate TPP primary coils are present in the system, each TPP secondary coil has to consider the impact from all of the three primary coils at all displacements. Given the inductances and mutual inductances for all possible displacements of the secondary, the power output of the system is a complex function of magnitudes and phases of the primary currents in the three TPP primary coils.

III. Control of IPT Systems With Multiple Primary Coils

A. Effective Coupling Factor as a Measurement of Power Transfer Capability

When CP–CP systems are compared with each other, the power transfer capability of the magnetic structures in each system can be compared in terms of k. From (11), a system with a higher k would be able to transfer a higher power than other systems when all of the system have equal S_{p}. For systems with multiple coils in the primary and the secondary, there is not a single k term that can be simply used to compare the power transfer capabilities of different systems. In order to be able to make comparisons in regards to power transfer capability between systems with different types of pads with varying numbers of coils, a term called effective coupling factor (k_{eff}) is used in this paper. This effective coupling factor is defined based on the ratio of total S_{p} in the primary to the total S_{u} in the secondary as shown in (26) here. S_{u} is deliberately used to find k_{eff} to eliminate the effects of the secondary electronics so that k_{eff} becomes a measurement of power transfer capability

$$\begin{bmatrix} V_{\mathrm{p1}} \\ V_{\mathrm{p2}} \\ V_{\mathrm{p3}} \\ 0 \\ 0 \\ 0 \end{bmatrix} = \begin{bmatrix} Z_{\mathrm{p1}} & 0 & 0 & j\omega M_{\mathrm{p1s1}} & j\omega M_{\mathrm{p1s2}} & j\omega M_{\mathrm{p1s3}} \\ 0 & Z_{\mathrm{p2}} & 0 & j\omega M_{\mathrm{p2s1}} & j\omega M_{\mathrm{p2s2}} & j\omega M_{\mathrm{p2s3}} \\ 0 & 0 & Z_{\mathrm{p3}} & j\omega M_{\mathrm{p3s1}} & j\omega M_{\mathrm{p3s2}} & j\omega M_{\mathrm{p3s3}} \\ j\omega M_{\mathrm{p1s1}} & j\omega M_{\mathrm{p2s1}} & j\omega M_{\mathrm{p3s1}} & Z_{\mathrm{s1}} & 0 & 0 \\ j\omega M_{\mathrm{p1s2}} & j\omega M_{\mathrm{p2s2}} & j\omega M_{\mathrm{p3s2}} & 0 & Z_{\mathrm{s2}} & 0 \\ j\omega M_{\mathrm{p1s3}} & j\omega M_{\mathrm{p2s3}} & j\omega M_{\mathrm{p3s3}} & 0 & 0 & Z_{\mathrm{s3}} \end{bmatrix} \begin{bmatrix} I_{\mathrm{p1}} \\ I_{\mathrm{p2}} \\ I_{\mathrm{p3}} \\ I_{\mathrm{s1}} \\ I_{\mathrm{s2}} \\ I_{\mathrm{s3}} \end{bmatrix}. \tag{16}$$

of only the magnetic structures

$$k_{\text{eff}} = \sqrt{\frac{S_{\text{u total}}}{S_{\text{p total}}}}. \tag{26}$$

From (3) and (16), $S_{\text{u total}}$ of a TPP–TPP can be found as shown in (27), while $S_{\text{p total}}$ is shown in (24):

$$S_{\text{u total}} = \sum_{n=1}^{3} S_{\text{un}} = \left| \sum_{m=1}^{3} \sum_{n=1}^{3} \omega L_{\text{pm}} I_{\text{pm}}^2 k_{\text{pmsn}}^2 \right|. \tag{27}$$

The subscripts "m" and "n" are used to denote different TPP primary or secondary coils, respectively. Similar to P_{out} shown in (25), $S_{\text{u total}}$ is also a function of only the primary currents if all of k and the inductances in the system are assumed to be constant. Depending on the k between the primary and the secondary, some combinations of the primary current magnitudes and phases result in a higher $S_{\text{u total}}$ for a lower S_{p}, which subsequently results in a higher k_{eff}. This means that finding the primary current magnitudes and phases resulting in the highest k_{eff} becomes an optimization problem. In cases where there is only a single coil in the primary and a single coil in the secondary, k_{eff} is the identical to k.

B. Exhaustive Search Controller

The method used in this paper to determine the optimal primary current magnitudes and phases is to use an exhaustive search controller [32], [35], [36]. The exhaustive search controller takes all of the variables in the system (k, L_{p}, L_{s}, and ω) and then computes all the possible k_{eff} for every combination of I_{p}. Once all the possible k_{eff} are found by the controller, the combination of the primary currents that results in the highest k_{eff} while meeting the power output requirements is used to energize the primary coils. This process of finding the optimal k_{eff} needs to be conducted every time there is a change to any one of the variables. For the purposes of this paper, k, L_{p}, L_{s}, and ω are assumed to be known at all times for all displacements of the secondary, since detecting displacement and changes to variables such as k and L are deemed outside the scope of this investigation.

An example flowchart of such an exhaustive search controller used in this paper is shown in Fig. 6. Here, $|I_{\text{p}}|$ and θ_{p} represent the magnitude and phase of the primary currents, respectively. The step sizes and the minimum and maximum bounds of $|I_{\text{p}}|$ and θ_{p} of the controller used in this paper are shown in Table I. The step size for the evaluation of the primary current magnitudes and phases in Table I was chosen as a balance between computational time, ensuring that the controller is able to locate the set of primary currents that achieve a working k_{eff} close to the ideal maximum k_{eff}.

In many high-power IPT systems, the energization of the primary pad is the major source of leakage magnetic flux. The controller presented here searches for the optimal primary currents that result in the lowest S_{p}, which helps in reducing leakage magnetic flux as discussed in Section IV. However, it should be noted that the combination of primary currents that result in the highest k_{eff} does not necessarily result in the most efficient operation, as the controller shown in Fig. 6 only prioritizes energizing primary coils that have high magnetic couplings to the secondary. With addition of switches in the secondary, the Q_{s} could be controlled rather than being determined by V_{out}, as shown in [37]. The controller could be refined to consider Q_{s}, efficiency as well as k_{eff} in the future; however, it is deemed outside the scope of this paper.

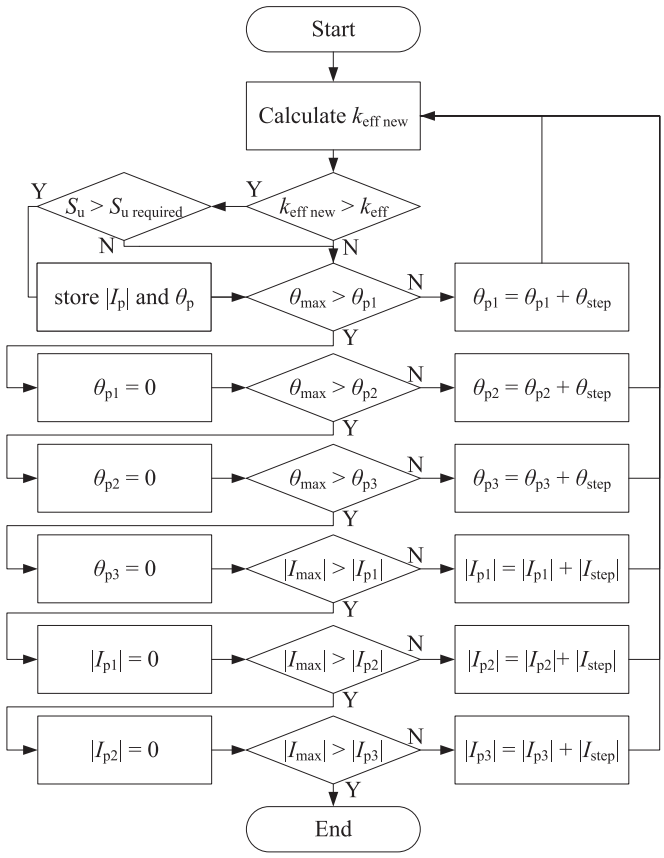

Fig. 6. Flowchart of an exhaustive controller searching for the highest k_{eff}.

TABLE I
CONTROLLER PARAMETERS FOR PRIMARY CURRENTS FOR k_{eff} OPTIMIZATION

Variable	Min	Max	Step
$\lvert I_{\text{p1}}\rvert$	0	92	1
$\lvert I_{\text{p2}}\rvert$	0	92	1
$\lvert I_{\text{p3}}\rvert$	0	92	1
θ_{p1}	0	180	30
θ_{p2}	0	180	30
θ_{p3}	0	180	30

C. Controller for the Highest Power Transfer

If the previous controller for the highest k_{eff} was to measure the power transfer capability, a controller for actually transferring power to the secondary needs to include the secondary electronics. The equation for P_{out} for a TPP–TPP system can be derived from (17)–(25) into the equation shown in (28). The magnetic losses are ignored in this equation for simplicity as

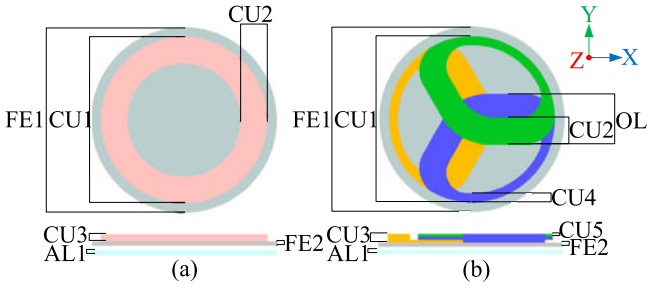

Fig. 7. Top and front views for (a) the CP and (b) the TPP with dimension labels.

they are relatively small

$$P_{\text{out}} = \left| V_{\text{out}} \sum_{n=1}^{3} \frac{\sum_{m=1}^{3} j\omega M_{\text{pmsn}} I_{\text{pm}}}{j\omega L_{\text{sn}}} \right|. \tag{28}$$

Here, V_{out}, which is set by the switch-mode controller, is now a factor in the equation as well as the primary currents. Using P_{out} as the optimization objective instead of k_{eff} and assuming that V_{out} stays constant at the desired nominal battery voltage, the same exhaustive search controller from Section III-B can be used to find the optimal primary currents for the highest power transfer for the least effort from the primary (S_{p}).

Note that unlike the controller for k_{eff}, the secondary is connected to a load, and therefore, Q_{s} of each of the TPP secondary coils varies depending on the value of V_{out} set by the switch-mode controller and V_{oc} induced by the primary, as shown in (20). In a parallel-tuned secondary, the TPP secondary coils that have lower V_{oc} induced in them would naturally increase their Q_{s} to compensate for the lower V_{oc} compared to coils in the other coils that have higher V_{oc}. In this paper, the exhaustive search controller did not consider any combinations of primary currents that resulted in a Q_{s} of higher than 10 in any of the secondary coils to keep the system from being too sensitive and minimize the losses in the coils. While it is not implemented in this paper, the secondary coils with relatively low V_{oc} that subsequently transfer low power to the load can be turned OFF to minimize the losses rather than running the secondary coils at high Q_{s}.

IV. Simulation of Magnetic Pads

The simulations in this paper investigate both k_{eff} and B_{leak} generated by CP–CP, CP–TPP, TPP–CP, and TPP–TPP systems. The simulation models for the TPP and the CP with dimension labels are shown in Fig. 7, and the corresponding dimensions are labeled in the Appendix. The ferrite and aluminum plates of both systems were designed to be the same dimensions for simplicity. The aluminum plate is placed underneath the ferrite to shield B_{leak} and to preserve structural rigidity of the pads. The surface area, copper, ferrite, and aluminum volume of both systems have been designed to be as similar as possible to ensure a fair comparison. The primary and secondary coil sizes were deliberately matched in this analysis to ensure good coupling [27]. The CP primary was then sized with a similar area to other higher power topologies under consideration in standards work

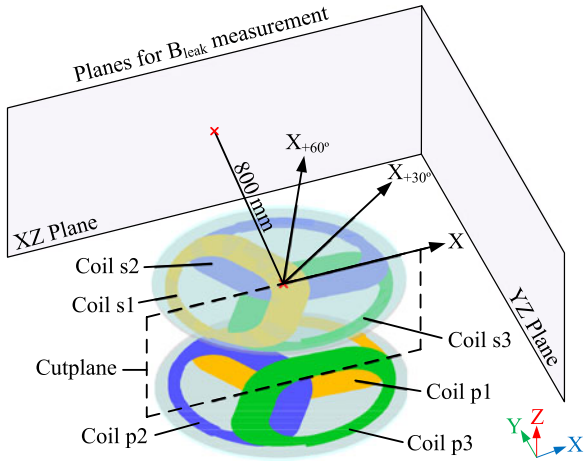

Fig. 8. Simulation model of TPP–TPP showing the different directions of displacement and the planes for B_{leak} measurement.

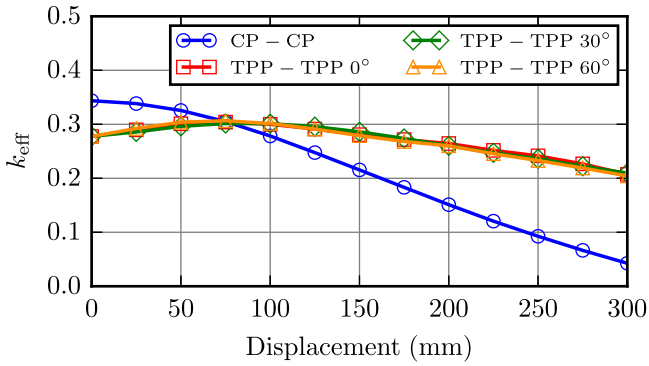

Fig. 9. k_{eff} for CP–CP and TPP–TPP at 150-mm air gap.

[38], while ensuring that it met the highest power level (WPT4) likely to be considered necessary in future around 20 kW to the load at the designed air gap and within desired tolerances. The sizes of the TPP primary and secondary were then matched to the CP using the same ferrite and copper volumes to enable the two topologies to be fairly compared. Further size optimization, which beyond the scope of this paper, naturally should be undertaken based on the desired tolerances and requirements to ensure that power can be delivered to the various sized vehicle pads presently under investigation by manufacturers at the various power ranges and air gaps expected.

For the simulations, the ideal alignment is where the center of the primary and the secondary is vertically centered with each other with a 150-mm air gap. Since the TPP is not perfectly symmetrical like the CP in every direction, misalignment performances are measured at three different angles (0°, 30°, and 60°) respective to the X-axis, as shown in Fig. 8. All simulations are carried out at an operating frequency of 85 kHz.

A. Effective Coupling Factor

The simulated k_{eff} between the CP–CP, CP–TPP, TPP–CP, and TPP–TPP systems described above for 20 kW of power transfer are shown in Figs. 9–11. In a CP–CP system, k_{eff} peaks at ideal alignment and then decreases as the CP secondary is

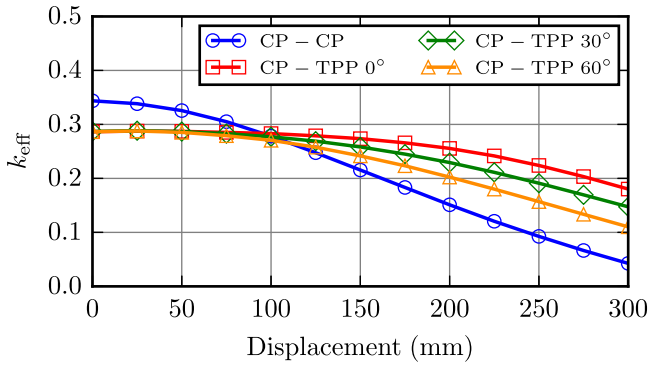

Fig. 10. k_{eff} for CP–CP and CP–TPP at 150-mm air gap.

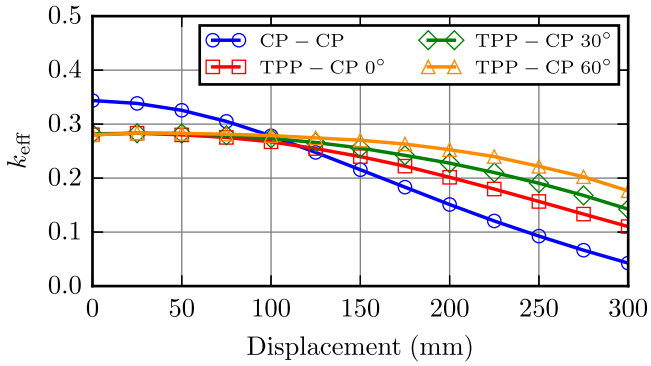

Fig. 11. k_{eff} for CP–CP and TPP–CP at 150-mm air gap.

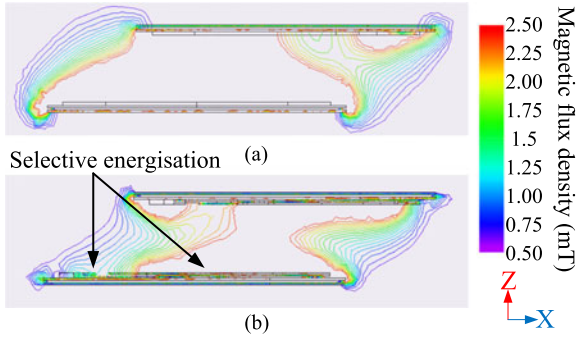

Fig. 12. Magnetic field density (RMS) of a cutplane along the X-axis of (a) CP–CP and (b) TPP–TPP at a secondary displacement of 200 mm.

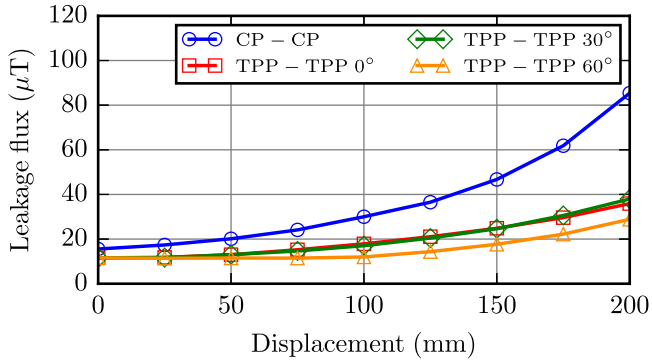

Fig. 13. B_{leak} for CP–CP and TPP–TPP for 20 kW at 150-mm air gap.

displaced further away from ideal alignment. In Figs. 9–11, a larger misalignment of 300 mm is shown to present an example of the power transfer capability of the TPP–TPP system at extreme misalignments. However, other results shown in this paper focus on misalignments up to 200 mm as the k_{eff} of some topologies decrease to a very low level at extreme misalignments that prevents any meaningful power transfer without generating a very high leakage magnetic flux.

Without misalignment, the CP–CP system achieves a higher k_{eff} than the TPP–TPP system. However, the TPP primary utilizes the controller described in Section III-B to generate different magnetic field shapes for all displacements of the TPP secondary, and this ensures a high and relatively flat k_{eff} profile for the TPP–TPP system. k_{eff} does not decrease below 0.2 for the TPP–TPP even at worst-case secondary displacement of 300 mm in any direction, as shown in Fig. 9, which ensures lower stress on the primary electronics and reduces B_{leak}, as discussed later. This shows that TPP–TPP systems have a high power transfer capability in any direction especially in cases where the secondary is prone to misalignment.

The k_{eff} of systems using the CP-TPP and the TPP-CP are similar, as shown in Figs. 10 and 11, since the only difference between the two systems is that the primary pad and the secondary pads are switched over. Both CP–TPP and TPP–CP systems show improved k_{eff} to the CP–CP system when the secondary is displaced. However, the k_{eff} of the CP–TPP and TPP–CP systems are more sensitive to the direction of the secondary displacement in contrast to the TPP–TPP system, which is agnostic to the direction of the displacement in the system.

Examples of the RMS magnetic field density of the CP–CP and the TPP–TPP systems transferring 20 kW are shown when the secondary is displaced by 200 mm in the X-direction in Fig. 12. The magnetic field density plots are based off the cutplane in the XZ plane shown in Fig. 8. Since the CP primary only has a single coil, the entire coil needs to be energized regardless of the displacement of the secondary, as shown in Fig. 12(a). As noted earlier, the TPP primary selectively energizes the coils that have higher individual magnetic coupling to the secondary, as shown in Fig. 12(b), which results in higher k_{eff} and lower B_{leak}.

B. Leakage Magnetic Field

Simulation results of B_{leak} of CP–CP, CP–TPP, TPP–CP, and TPP–TPP systems transferring 20 kW are shown up to 200-mm displacement in Figs. 13–15. V_{out} is set to be 360 V for both CP–CP and TPP–TPP systems. B_{leak} is measured at XZ and YZ planes 800 mm away from the center of the secondary as shown in an example illustration in Fig. 8.

B_{leak} of the CP–CP system shown in Fig. 13 is much higher than that of the TPP–TPP system at all displacements. The difference in B_{leak} between the two systems is increased as the secondary is displaced further away from the ideal alignment. At the worst-case displacement of 200 mm, the TPP–TPP system has 56% lower B_{leak} than the CP–CP system. This difference in

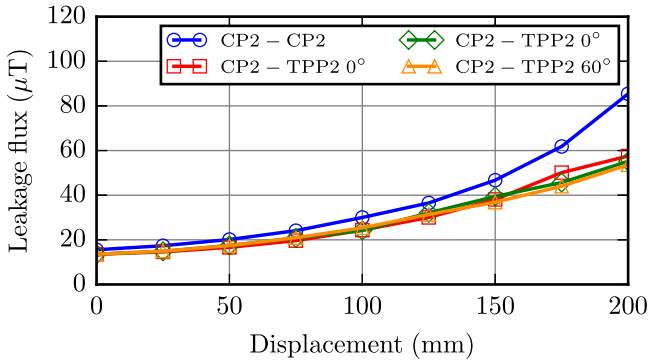

Fig. 14. B_{leak} for CP–CP and CP–TPP for 20 kW at 150-mm air gap.

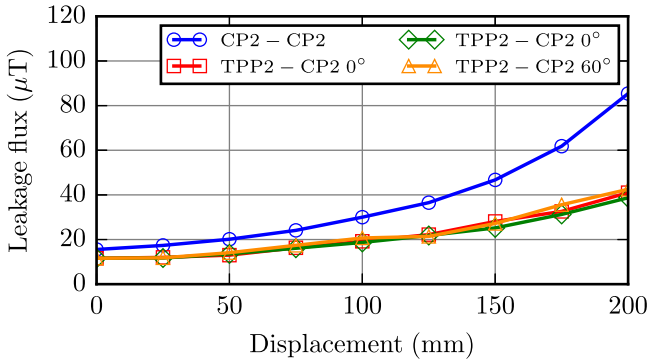

Fig. 15. B_{leak} for CP–CP and TPP–CP for 20 kW at 150-mm air gap.

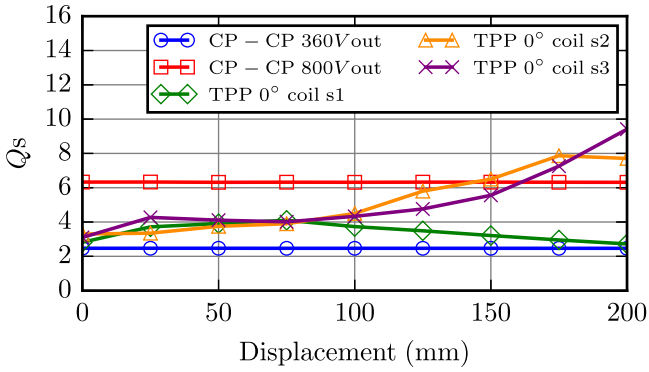

Fig. 16. Q_{s} for CP–CP and TPP–TPP 0° for 20 kW at 150-mm air gap.

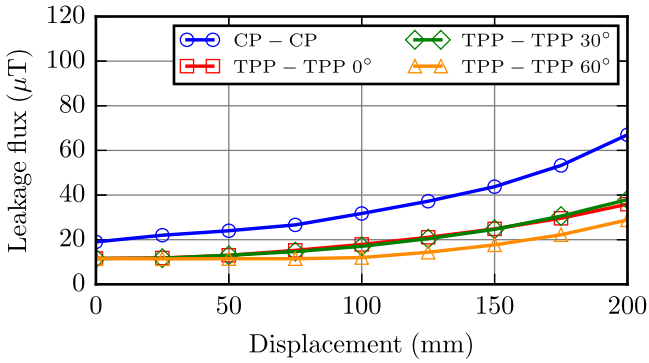

Fig. 17. B_{leak} for CP–CP at 800 V V_{out} and TPP–TPP at 360 V V_{out} for 20 kW at 150-mm air gap.

B_{leak} can be attributed to the selective energization, shown in Fig. 12, for two reasons. First, the secondary pad acts as a natural cover to limit the potential B_{leak} when it is placed on top of a primary pad. As the secondary is displaced away from the ideal alignment, more and more parts of the primary pad are exposed to generate B_{leak}. The CP primary needs to energize the entire coil, so the exposed parts of the CP primary increase B_{leak}. This is not the case for the TPP primary as the exhaustive controller energizes TPP coils closer to the secondary more than the TPP coils further away from the secondary by design. In conjunction with this, the TPP–TPP system requires less total S_{p} than the CP–CP system since the TPP–TPP system has higher k_{eff} at misaligned positions, which leads to even further reductions in B_{leak}.

While k_{eff} for CP–TPP and TPP–CP are similar as shown previously, the B_{leak} generated from the TPP–CP system can be as much as 30% lower than the CP–TPP system at 200-mm displacement, as shown in Figs. 14 and 15. This reduction in B_{leak} is possible because of the way in which the TPP primary coils are selectively energized, as shown in Fig. 12, which is not possible in a single-coil primary.

The Q_{s} of the CP–CP and TPP–TPP system for each of the secondary coils are shown in Fig. 16. Previously, it was shown that Q_{s} of the CP–CP system is directly proportional to V_{out}, as shown in (15). For example, Q_{s} of the CP–CP system is approximately 2.5; however, increasing V_{out} to 800 V increases Q_{s} of the CP–CP system to approximately 6.3, as shown in Fig. 16. The Q_{s} of the CP–CP system stays constant throughout all of the secondary displacements, since the primary controller assumes V_{out} to be fixed and is designed to increase its primary current magnitude to compensate for the decrease in magnetic coupling from misalignment.

In the TPP–TPP system, even though V_{out} is constant, the individual Q_{s} of the TPP secondary coils change depending on the primary currents and the magnetic couplings between the coils, as described in (20). The variation in Q_{s} of each of the TPP secondary coils is shown in Fig. 16 as the secondary is displaced in 0° direction. Near the ideal alignment, the individual magnetic coupling of the TPP primary to TPP secondary is relatively similar. The controller energizes the primary currents at similar levels, so all of the TPP secondary coils are at similar values of Q_{s}. Near the worst-case secondary displacement of 200 mm in the X-direction, only coil s1 has high magnetic coupling to the TPP primary, which results in coils s2 and s3 resonating up to a higher Q_{s}. Coil s1 maintains a high coupling to the secondary at all displacements in the X-direction, so the coil does not reach a high value of Q_{s}. As shown, the TPP secondary coils have varying Q_{s} between the coils that cannot be directly controlled if V_{out} is to be set to a constant value unlike the CP secondary.

A new plot of B_{leak} of the CP–CP system with V_{out} set to 800 V is shown in Fig. 17 and compared against the previous results from the TPP–TPP system at V_{out} of 360 V to show how a CP–CP system with a higher Q_{s} would perform. This increase in Q_{s} of the CP–CP system shifts some of the S_{p} into S_{s}, which results in a decrease in B_{leak} at misaligned positions. However,

TABLE II
DISTRIBUTION OF REAL AND APPARENT POWER IN CP–CP AND TPP–TPP SYSTEMS*

	CP–CP 360 V_{out}		CP–CP 800 V_{out}		TPP–TPP 0° 360 V_{out}							
(mm)	(kVA)	(kW)	(kVA)	(kW)	(kVA)			(kW)	(kVA)			(kW)
Disp.	S_{p}	P_{p}	S_{p}	P_{p}	S_{p1}	S_{p2}	S_{p3}	$S_{\text{p total}}$	P_{p1}	P_{p2}	P_{p3}	$P_{\text{p total}}$
100	99.74	20.83	42.95	21.26	26.31	5.96	28.25	60.52	8.56	3.09	9.59	21.24
Disp.	S_{s}	P_{s}	S_{s}	P_{s}	S_{s1}	S_{s2}	S_{s3}	$S_{\text{s total}}$	P_{s1}	P_{s2}	P_{s3}	$P_{\text{s total}}$
100	53.76	20.19	129.15	20.19	35.69	33.98	32.64	102.31	8.27	5.91	5.94	20.12
Disp.	S_{p}	P_{p}	S_{p}	P_{p}	S_{p1}	S_{p2}	S_{p3}	$S_{\text{p total}}$	P_{p1}	P_{p2}	P_{p3}	$P_{\text{p total}}$
150	169.51	22.06	68.55	21.29	28.39	3.22	35.31	66.92	7.68	1.62	12.13	21.43
Disp.	S_{s}	P_{s}	S_{s}	P_{s}	S_{s1}	S_{s2}	S_{s3}	$S_{\text{s total}}$	P_{s1}	P_{s2}	P_{s3}	$P_{\text{s total}}$
150	53.76	20.19	129.14	20.17	34.83	35.09	32.64	102.56	9.91	4.44	5.84	20.19

*The values in this table are derived from the data shown in Figs. 9 and 16.

a higher S_{s} in the CP–CP system now results in a higher B_{leak} at ideal alignment, which shows that there is a tradeoff to be made between Q_{s} and B_{leak}. Even with the higher Q_{s} in the CP–CP system, the TPP–TPP system has a much lower B_{leak} at all displacements. At the worst-case displacement of 200 mm, B_{leak} of the TPP–TPP system with V_{out} of 360 V is 43% lower than the CP–CP system with V_{out} of 800 V.

C. Distribution of Real and Apparent Power

The breakdown of the real and apparent power in the primary and secondary pads as calculated from simulations for both the CP–CP and TPP–TPP systems is shown in Table II. This table provides an idea of the necessary component ratings for the resonant circuits, rectifiers, and H-bridges, assuming that the systems were designed to transfer 20 kW up to either 100- or 150-mm displacements. Note that the various coils of the TPP primary and secondary have different contributions to the transfer of power when the secondary is displaced in different directions. In some cases, one primary coil may provide a stronger magnetic coupling to the secondary, but the coupling in other coils may be higher at displacements in the opposite direction. As such, all coils and components would need to be rated identically at the upper limit of the ratings identified.

If both of the systems had a nominal battery voltage (V_{out}) set to 360 V and secondary displacement of 100 mm, the component ratings in the TPP–TPP for each of the H-bridges and rectifiers would be around half of the CP–CP, and the ratings of the primary resonant circuits would be around a third of the CP–CP. When the displacement is increased up to 150 mm, the ratings for the components in the TPP-TPP system increase slightly, since the system now relies more on coils with higher magnetic coupling to transfer power.

If the V_{out} of the CP–CP system was designed to be 800 V, the majority of the apparent power in the CP primary would be shifted to the CP secondary due to the increase in Q_{s}, as shown in Fig. 16. This makes the total apparent power in the primary and the secondary pads similar for both systems at displacements up to 150 mm. In this case, the power rating for H-bridges and rectifiers for the TPP–TPP remain at around half of the CP–CP. However, each of the TPP primary resonant circuit is now rated to be half of the CP primary, while the secondary resonant circuit of the TPP is around a quarter of the CP. This shows that while the TPP–TPP system requires more number of components, the components ratings are lower than the CP–CP system while providing benefits in B_{leak}, as shown previously.

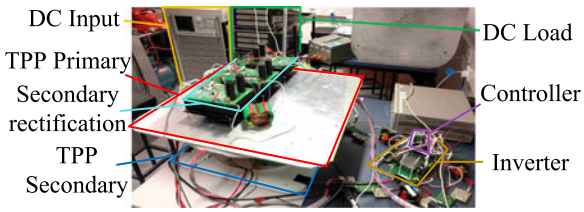

Fig. 18. Experimental setup of the prototype TPP–TPP system in the laboratory.

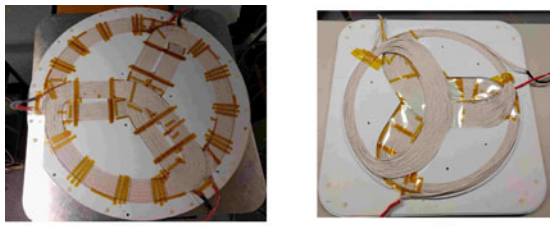

Fig. 19. Experimental setup of the prototype (a) TPP primary and (b) TPP secondary in the laboratory.

V. EXPERIMENTAL VALIDATION

The setup of the prototype system in the laboratory, which was used to validate the accuracy of the simulation tool used in Section IV, is shown in Fig. 18. Due to the availability of resources, prefabricated TPPs were used for experimental validation, as shown in Fig. 19. The TPP primary is shown in Fig. 19(a) and the TPP secondary is shown in Fig. 19(b). The dimensions of the prototype TPP primary and secondary are shown in Table III. Due to the changes in dimensions, a new set of simulations were conducted using the dimensions of the prototype TPP in Table III.

In Fig. 20, k_{eff} of the prototype and simulated TPP–TPP systems are compared. The air gap between the TPP primary and the TPP secondary is set to be 200 mm. Salient coupling factors between the TPP primary and the TPP secondary are

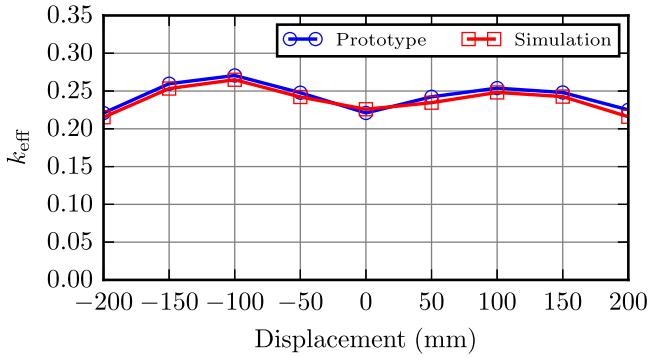

Fig. 20. k_{eff} for prototype and simulated TPP–TPP systems.

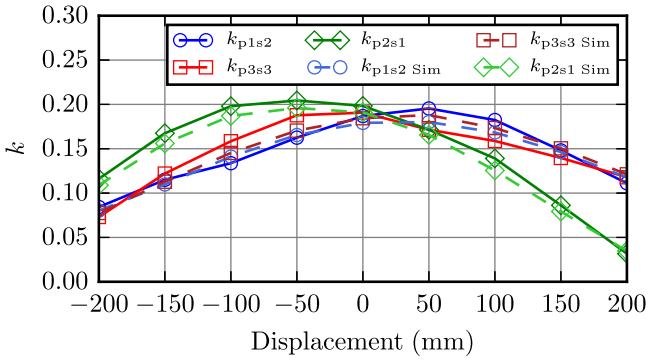

Fig. 21. k for prototype and simulated TPP–TPP systems.

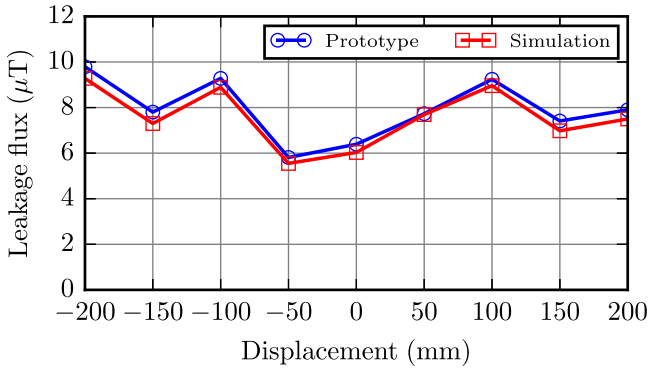

Fig. 22. B_{meas} for prototype and simulated TPP–TPP systems for 2 kW.

shown in Fig. 21. The individual coupling factors and k_{eff} are in good agreement for the laboratory prototype and the simulation.

In Fig. 22, B_{meas} of the prototype TPP–TPP system is measured and compared with the simulation results. For precise measurements, B_{meas} is measured at a fixed point 800 mm in the Y-direction from the center of the primary pad. Note that B_{meas} is not smoothly increasing or decreasing, since the controller is constantly changing the primary coil magnitudes and phases depending on the displacement of the secondary. The agreement of leakage magnetic field between the prototype and the simulation results validates the simulation tool.

Fig. 23 shows the primary currents of the prototype and simulated TPP–TPP systems when the secondary is ideally aligned. The current magnitudes and phases are determined by the

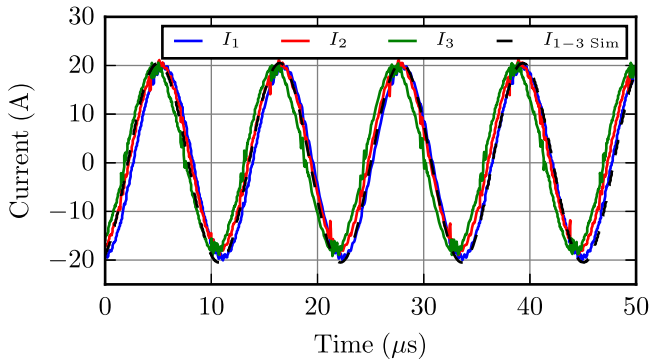

Fig. 23. I_{1-3} for prototype and simulated TPP–TPP systems for 2 kW at 0-mm displacement.

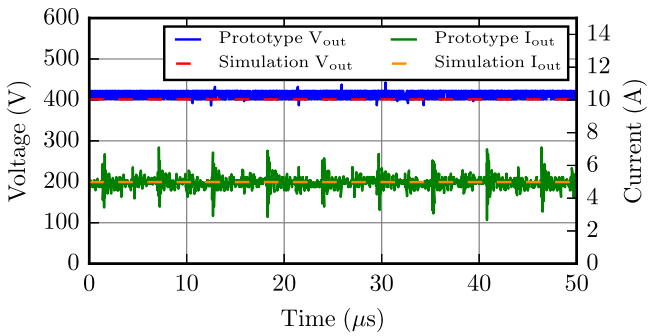

Fig. 24. I_{1-3} for prototype and simulated TPP–TPP systems for 2 kW at 0-mm displacement.

controller discussed previously in Section IV. The controller found the optimal primary current magnitude to be 14.5 A and no phase difference between the three primary currents. In Fig. 24, V_{out} and I_{out} are shown for the prototype and simulated TPP–TPP systems. The switch-mode controller was designed to set V_{out} to be 400 V, and efficiency from the dc input to the inverters to the dc output to the load is 87% at this displacement.

VI. Conclusion

In this paper, a TPP was evaluated against a CP with both pads designed for 20-kW power transfer. The paper evaluates all possible configurations including CP–CP, CP–TPP, TPP–CP, and TPP–TPP. The TPP is a recently proposed magnetic structure using three mutually decoupled coils, in contrast to common magnetic structures using a single coil such as the CP or two coils. Mathematical models that account for the rectification and switch-mode controllers are used for both systems. Using the models, an exhaustive search controller was developed to maximize the effective coupling factor (k_{eff}) of the systems by controlling the primary current magnitudes and phases. The TPP–TPP system has shown that k_{eff} can be improved and is relatively flat irrespective of the displacement of the secondary compared to the CP–CP system. Both systems used a similar volume of copper, ferrite, and aluminum. The leakage magnetic field (B_{leak}) was also reduced in the TPP–TPP system for all displacements compared to the CP–CP system. The leakage can be reduced up to 43% at the worst-case misalignment, which

TABLE III
DIMENSIONS OF THE LABELS FOR EACH OF THE PAD SIZINGS FOR SIMULATION AND VALIDATION

Labels	Sim. CP	Sim. TPP	Lab TPP pri	Lab TPP sec
CU1	580	600	600	800
CU2	96	96	96	80
CU3	12	12	12	12
CU4	-	32	32	80
CU5	-	4	4	4
FE1	600	670	840	800
FE2	5	5	10	10
AL1	4	4	6	6
AL2	600	670	715	915
OL	-	96	170	175
A1	1	1	1	1

is essential as higher power systems up to 20 kW are being considered for development. The simulation tools used for the analysis were validated using a prototype system operating at 85 kHz in the laboratory, which resulted in a dc–dc efficiency of 87% at ideal alignment.

APPENDIX

Dimensions corresponding to the labels shown in Fig. 7 are shown in Table III for the simulation and prototype pads. The prototype TPP used rectangular ferrite blocks with dimensions of 125 mm $\times$ 100 mm $\times$ 10 mm. The ferrite pieces were cut or arranged to best resemble a circular ferrite sheet. The aluminum sheet underneath both of the prototype TPP is square shaped, as shown in Fig. 19.

REFERENCES

[1] G. Covic and J. Boys, "Modern trends in inductive power transfer for transportation applications," *IEEE J. Emerg. Sel. Topics Power Electron.*, vol. 1, no. 1, pp. 28–41, Mar. 2013.

[2] S. Hui, W. Zhong, and C. Lee, "A critical review of recent progress in mid-range wireless power transfer," *IEEE Trans. Power Electron.*, vol. 29, no. 9, pp. 4500–4511, Sep. 2014.

[3] S. Choi, B. Gu, S. Jeong, and C. Rim, "Advances in wireless power transfer systems for roadway-powered electric vehicles," *IEEE J. Emerg. Sel. Topics Power Electron.*, vol. 3, no. 1, pp. 18–36, Mar. 2015.

[4] S. Y. R. Hui, "Magnetic resonance for wireless power transfer [a look back]," *IEEE Power Electron. Mag.*, vol. 3, no. 1, pp. 14–31, Mar. 2016.

[5] J. T. Boys and G. A. Covic, "The inductive power transfer story at the university of auckland," *IEEE Circuits Syst. Mag.*, vol. 15, no. 2, pp. 6–27, Second Quarter 2015.

[6] P. Sergeant and A. Van den Bossche, "Inductive coupler for contactless power transmission," *IET Electr. Power Appl.*, vol. 2, no. 1, pp. 1–7, Jan. 2008.

[7] J. Hirai, T.-W. Kim, and A. Kawamura, "Study on intelligent battery charging using inductive transmission of power and information," *IEEE Trans. Power Electron.*, vol. 15, no. 2, pp. 335–345, Mar. 2000.

[8] W. Zhong, X. Liu, and S. Hui, "Analysis on a single-layer winding array structure for contactless battery charging systems with free-positioning and localized charging features," in *Proc. IEEE Energy Convers. Congr. Expo.*, Sep. 2010, pp. 658–665.

[9] J. T. Boys and A. W. Green, "Intelligent road-studs - lighting the paths of the future," *IPENZ Trans.*, vol. 24, no. 1, pp. 33–40, 1997.

[10] G. B. Joun and B. H. Cho, "An energy transmission system for an artificial heart using leakage inductance compensation of transcutaneous transformer," *IEEE Trans. Power Electron.*, vol. 13, no. 6, pp. 1013–1022, Nov. 1998.

[11] ICNIRP, "Guidelines for limiting exposure to time-varying electric and magnetic fields (1 Hz to 100 kHz)," *Health Phys.*, vol. 99, no. 6, pp. 818–836, 2010.

[12] M. Budhia, G. Covic, and J. Boys, "Design and optimization of circular magnetic structures for lumped inductive power transfer systems," *IEEE Trans. Power Electron.*, vol. 26, no. 11, pp. 3096–3108, Nov. 2011.

[13] M. Budhia, G. Covic, J. Boys, and C.-Y. Huang, "Development and evaluation of single sided flux couplers for contactless electric vehicle charging," in *Proc. IEEE Energy Convers. Congr. Expo.*, Sep. 2011, pp. 614–621.

[14] A. Zaheer, H. Hao, G. Covic, and D. Kacprzak, "Investigation of multiple decoupled coil primary pad topologies in lumped IPT systems for interoperable electric vehicle charging," *IEEE Trans. Power Electron.*, vol. 30, no. 4, pp. 1937–1955, Apr. 2015.

[15] H. Matsumoto, Y. Neba, K. Ishizaka, and R. Itoh, "Model for a three-phase contactless power transfer system," *IEEE Trans. Power Electron.*, vol. 26, no. 9, pp. 2676–2687, Sep. 2011.

[16] H. Sakamoto, K. Harada, S. Washimiya, K. Takehara, Y. Matsuo, and F. Nakao, "Large air-gap coupler for inductive charger [for electric vehicles]," *IEEE Trans. Magn.*, vol. 35, no. 5, pp. 3526–3528, Sep. 1999.

[17] D. Thrimawithana, U. Madawala, A. Francis, and M. Neath, "Magnetic modeling of a high-power three phase bi-directional IPT system," in *Proc. 37th Annu. Conf. IEEE Ind. Electron. Soc.*, Nov. 2011, pp. 1414–1419.

[18] M. Budhia, G. Covic, and J. Boys, "Magnetic design of a three-phase inductive power transfer system for roadway powered electric vehicles," in *Proc. IEEE Vehicle Power Propulsion Conf.*, Sep. 2010, pp. 1–6.

[19] J. Huh, S. Lee, W. Lee, G. Cho, and C. Rim, "Narrow-width inductive power transfer system for online electrical vehicles," *IEEE Trans. Power Electron.*, vol. 26, no. 12, pp. 3666–3679, Dec. 2011.

[20] G. Elliott, S. Raabe, G. Covic, and J. Boys, "Multiphase pickups for large lateral tolerance contactless power-transfer systems," *IEEE Trans. Ind. Electron.*, vol. 57, no. 5, pp. 1590–1598, May 2010.

[21] S. Raabe and G. Covic, "Practical design considerations for contactless power transfer quadrature pick-ups," *IEEE Trans. Ind. Electron.*, vol. 60, no. 1, pp. 400–409, Jan. 2013.

[22] M. Bertoluzzo, G. Buja, and H. K. Dashora, "Lumped track layout design for dynamic wireless charging of electric vehicles," *IEEE Trans. Ind. Electron.*, vol. 63, no. 10, pp. 6631–6640, Oct. 2016.

[23] S. Moon and G. W. Moon, "Wireless power transfer system with an asymmetric four-coil resonator for electric vehicle battery chargers," *IEEE Trans. Power Electron.*, vol. 31, no. 10, pp. 6844–6854, Oct. 2016.

[24] H. Kim *et al.*, "Coil design and measurements of automotive magnetic resonant wireless charging system for high-efficiency and low magnetic field leakage," *IEEE Trans. Microw. Theory Techn.*, vol. 64, no. 2, pp. 383–400, Feb. 2016.

[25] Z. H. Ye, Y. Sun, X. Dai, C. S. Tang, Z. H. Wang, and Y. G. Su, "Energy efficiency analysis of u-coil wireless power transfer system," *IEEE Trans. Power Electron.*, vol. 31, no. 7, pp. 4809–4817, Jul. 2016.

[26] S. Y. Choi, S. Y. Jeong, B. W. Gu, G. C. Lim, and C. T. Rim, "Ultraslim s-type power supply rails for roadway-powered electric vehicles," *IEEE Trans. Power Electron.*, vol. 30, no. 11, pp. 6456–6468, Nov. 2015.

[27] F. Y. Lin, G. Covic, and J. Boys, "Evaluation of magnetic pad sizes and topologies for electric vehicle charging," *IEEE Trans. Power Electron.*, vol. 30, no. 11, pp. 6391–6407, Nov. 2015.

[28] C. Y. Huang, J. E. James, and G. A. Covic, "Design considerations for variable coupling lumped coil systems," *IEEE Trans. Power Electron.*, vol. 30, no. 2, pp. 680–689, Feb. 2015.

[29] K. Aditya, V. K. Sood, and S. S. Williamson, "Magnetic characterization of unsymmetrical coil pairs using archimedean spirals for wider misalignment tolerance in IPt systems," *IEEE Trans. Transp. Electrific.*, vol. 3, no. 2, pp. 454–463, Jun. 2017.

[30] T. Yilmaz, N. Hasan, R. Zane, and Z. Pantic, "Multi-objective optimization of circular magnetic couplers for wireless power transfer applications," *IEEE Trans. Magn.*, vol. 53, no. 8, pp. 1–12, Aug. 2017.

[31] F. Y. Lin, G. A. Covic, and J. T. Boys, "Leakage flux control of mismatched IPT systems," *IEEE Trans. Transp. Electrification*, vol. 3, no. 2, pp. 474–487, Jun. 2017.

[32] S. Kim, G. Covic, and J. Boys, "Tripolar pad for inductive power transfer systems for EV charging," *IEEE Trans. Power Electron.*, vol. 32, no. 7, pp. 5045–5057, Jul. 2017.

[33] S. Kim, A. Zaheer, G. Covic, and J. Boys, "Tripolar pad for inductive power transfer systems," in *Proc. 40th Annu. Conf. IEEE Ind. Electron. Soc.*, Oct. 2014, pp. 3066–3072.

[34] A. Zaheer, G. A. Covic, and D. Kacprzak, "A bipolar pad in a 10-kHz 300-W distributed IPT system for AGV applications," *IEEE Trans. Ind. Electron.*, vol. 61, no. 7, pp. 3288–3301, Jul. 2014.
[35] S. Kim, A. Tejeda, G. A. Covic, and J. T. Boys, "Analysis on mutually decoupled primary coils for IPT systems for EV charging," in *Proc. IEEE Energy Convers. Congr. Expo.*, 2016, pp. 1–6.
[36] F. Y. Lin, S. Kim, G. Covic, and J. T. Boys, "Effective coupling factors for series and parallel tuned secondaries in IPT systems using bi-polar primary pads," *IEEE Trans. Transp. Electrific.*, vol. 3, no. 2, pp. 434–444, Jun. 2017.
[37] T. Diekhans and R. W. D. Doncker, "A dual-side controlled inductive power transfer system optimized for large coupling factor variations and partial load," *IEEE Trans. Power Electron.*, vol. 30, no. 11, pp. 6320–6328, Nov. 2015.
[38] *Wireless Power Transfer for Light-Duty Plug-In/Electric Vehicles and Alignment Methodology*, SAE TIR J2954, May 2016.

Seho Kim (S'14) received the B.E. (Hons.) degree in electrical and electronics engineering in 2012 from the University of Auckland, Auckland, New Zealand, where he is currently working toward the Ph.D. degree.

His current research interests include the design of inductive power transfer (IPT) systems, particularly in multiphase IPT systems for charging robots and electric vehicles.

Grant A. Covic (S'88–M'89–SM'04) received the B.E. (Hons.) and Ph.D. degrees in electrical and electronic engineering from the University of Auckland (UoA), Auckland, New Zealand, in 1986 and 1993, respectively.

He became a full-time Lecturer in 1992, a Senior Lecturer in 2000, an Associate Professor in 2007, and a Professor in 2013 with the Department of Electrical and Computer Engineering, UoA. In 2010, he cofounded (with Prof. J. Boys) a new global start-up company HaloIPT focusing on electric vehicle (EV) wireless charging infrastructure, which was sold in late 2011. He currently heads power electronics research at the UoA and co-leads the interoperability subteam within the SAE J2954 wireless charging standard for EVs. He has published more than 100 refereed papers in international journals and conferences. He holds a number of US patents with many more pending, from which licenses in specialized application areas of nductive (contactless) power transfer (IPT) have been granted around the world. His research and consulting interests include power electronics, electric vehicle battery charging, and IPT.

Dr. Covic is a Fellow of the Institution of Professional Engineers New Zealand. He (together with Prof. Boys) received the New Zealand Prime Minsters Science Prize, the KiwiNet Research Commercialisation Award, and the Vice Chancellors Commercialisation Medal for his work in IPT.

John T. Boys received the M.E. degree from the University of Auckland, Auckland, New Zealand, in 1965.

After completing his Ph.D., he was with SPS technologies for five years before returning to academia as a Lecturer with the University of Canterbury. In 1977, he moved to the University of Auckland, where he developed his work in power electronics. He is currently a Distinguished Professor Emeritus with the Department of Electrical and Computer Engineering, The University of Auckland, and co-Founder of HaloIPT. He has authored or coauthored more than 100 papers in international journals. He is the holder of more than 40 U.S. patents, from which licenses in specialized application areas have been granted around the world. His specialist research areas are power electronics and electromagnetics for inductive power transfer, where he works with Prof. G. A. Covic.

Dr. Boys is a Fellow of the Royal Society of New Zealand and a Distinguished Fellow of the Institution of Professional Engineers New Zealand.